Published in final edited form as:
J Opt Soc Am A Opt Image Sci Vis. 2009 February ; 26(2): 376–386.

Partially coherent illumination in full-field interferometric synthetic aperture microscopy

Daniel L. Marks, **Brynmor J. Davis**, **Stephen A. Boppart**, and **P. Scott Carney***
Beckman Institute for Advanced Science and Technology and the Department of Electrical and Computer Engineering, University of Illinois at Urbana-Champaign, 405 North Mathews, Urbana, Illinois 61801, USA

Abstract

A model is developed for optical coherence tomography and interferometric synthetic aperture microscopy (ISAM) systems employing full-field frequency-scanned illumination with partial spatial coherence. This model is used to derive efficient ISAM inverse scattering algorithms that give diffraction-limited resolution in regions typically regarded as out of focus. Partial spatial coherence of the source is shown to have the advantage of mitigating multiple-scattering effects that can otherwise produce significant artifacts in full-field coherent imaging.

1. INTRODUCTION

Interferometric synthetic aperture microscopy (ISAM) [1–9] is a method of tomographic optical microscopy that brings the power of computed imaging and inverse scattering together with interferometric broadband optical imaging. ISAM provides spatially invariant resolution of objects in an extended three-dimensional volume including regions away from the focus of the objective. This result is achieved using a quantitative estimation of the inhomogeneities in the refractive index or susceptibility of an object. The solution of the inverse problem for ISAM has been found for many scanning geometries and types of illumination, including low [3] and high numerical aperture scanned-beam [4,5], rotationally-scanned-beam catheter [7], and full-field illumination [8]. In all these cases, it is assumed that the illumination source is spatially coherent (single mode), but temporally incoherent, or broadband. In general, sources of illumination in microscopy are partially spatially coherent [10,11], motivating this study of partially coherent illumination in ISAM.

ISAM and optical coherence tomography (OCT) use low-coherence interferometry to achieve label-free optical imaging based on the scattering properties of an object. In tissue, ISAM and OCT are typically applied in the near infrared region of the electromagnetic spectrum, as in this range the optical response of tissue is dominated by scattering rather than absorption. The interferometric methodology employed allows a high-resolution three-dimensional image to be collected in highly scattering tissues, with a favorable depth of penetration for an optical modality. Early OCT systems employed confocal data collection and time-domain coherence ranging. As a result, constructing a three-dimensional image required two-dimensional transverse sampling of the object (using, for example, object translation or beam scanning) and one-dimensional scanning of the interferometer reference arm. It has since been shown that the reference arm need not be scanned if the source can be spectrally scanned (using either a swept source or spectral detection), resulting in significantly improved collection times and

* *Corresponding author: carney@uiuc.edu* .

instrument sensitivity [12,13]. An array detector and full-field illumination can also be used to simultaneously measure a signal from multiple transverse locations simultaneously, thus eliminating the need for transverse scanning [14–28]. However, confocal detection has the advantage that much of the light that is multiply scattered in the sample is rejected at the detector pinhole. Mitigation of the strong multiple-scatter artifacts expected in full-field ISAM is a practical motivation for the work presented here.

Beyond the fact that real sources are necessarily partially spatially coherent to some extent, in conventional microscopy and OCT the coherence properties of the illumination may be manipulated to suppress or enhance various interference phenomena. In particular, decreasing the spatial coherence of the source generally reduces the interference signal produced by multiply scattered light [29,30]. Because images are formed in OCT in principle from the singly backscattered signal, the multiply scattered light can contribute unwanted distortion and apparent noise to the resulting image [31–34].

In a previously published paper [8], a solution of the full-field inverse scattering problem was derived for the case that the source of illumination is fully spatially coherent. In general, the solution of the inverse scattering problem for interferometric full-field microscopy depends on the spatial coherence of the illumination source, therefore the prior work [8] is not applicable to the case of partially coherent illumination. In this work, the solution of the inverse scattering problem is derived for data available in experiments utilizing the instrumentation of full-field OCT or optical coherence microscopy for the case that partially spatially coherent illumination sources are used. Through analysis and simulation, the role of the source coherence in the solution is demonstrated and it is seen that the use of partially coherent sources offers certain advantages.

To explore the operation of a full-field interferometric microscope with partially coherent illumination, the instrument shown in Fig. 1 is proposed and analyzed. In the proposed design, the source is of variable spatial coherence. When the source is set to be at the fully spatially coherent limit, the setup is similar to the instrument of the earlier study [8] and the earlier results are applicable.

The portion of Fig. 1 labeled “partially coherent illumination,” is discussed below. The illumination consists of a spatially incoherent source, an iris placed in front of the source to vary the apparent size of the source, and a collimation lens to collimate the illumination. An example of a spatially incoherent source is the filament of an incandescent light bulb. Each point on the filament surface radiates a randomly fluctuating electromagnetic field, such that the fields radiated by different regions on the filament surface do not interfere when averaged over a long time interval. Another example is a spatially coherent monochromatic laser, with its spatial coherence modified by a spinning or translating diffuser [10]. Such a source produces quasi-monochromatic, spatially incoherent light. The light emanating from points on the surface of the incoherent source is collimated by the collimation lens so that the radiating source points produce mutually incoherent plane waves. Such illumination is akin to Koehler illumination [35] in a conventional microscope, in contrast to critical illumination when the incoherent source surface is imaged onto the sample. By adjusting the size of the iris, the spatial coherence can be varied from very low (when the iris is opened), to very high (when the iris is closed).

The part of Fig. 1 corresponding to the interferometer is detailed below. The interferometer is of a Michelson type and consists of reference and sample paths. A 50/50 beam splitter divides the illumination field between these paths. As shown in Fig. 1, both the reference and sample fields are demagnified by telescopes of magnification factor M. In the sample relay telescope, a pupil limits the spatial bandwidth of the field collected from the sample. The sample relay

telescope afocally and telecentrically relays the field from the source field plane to the sample plane with demagnification. The sample scatters the field backwards through the sample relay telescope, where it reflects off the beam splitter and onto the focal plane array. The focal plane array is placed so that the sample relay telescope afocally and telecentrically images the sample plane to the focal plane array. The reference beam begins at the beam splitter and is relayed by the reference delay telescope to the reference delay mirror. The reference delay telescope afocally and telecentrically images the source field plane to the reference mirror plane. The field that reflects off the mirror is imaged afocally and telecentrically onto the focal plane array. The intensity of the interference pattern produced by the superimposed reference and sample signals is measured by the focal plane array. In practice, a Fizeau-type interferometer where the reference beam is returned from a reflective planar surface placed in front of the sample avoids the need for a separate reference telescope to relay the reference field.

The source of illumination is taken to be spatially incoherent, quasi-monochromatic, and of tunable temporal central frequency [13,36]. Data are acquired by tuning the wavelength of the source while recording the intensity of interferograms on the focal plane array. From these interferograms, the susceptibility of the sample is inferred. In Section 2, a general forward model is derived that is applicable to partially coherent full-field OCT and will serve as the basis for partially coherent ISAM. In Section 3, a linear solution for the inverse scattering problem for partially coherent illumination is derived. The effects of multiple scattering are considered in Section 4 and simulated experiments are presented in Section 5.

2. FORWARD MODEL FOR PARTIALLY COHERENT FULL-FIELD OPTICAL COHERENCE TOMOGRAPHY

A. General Case

The objective in formulating the forward problem is to derive an expression for the data in terms of the unknown object susceptibility. The raw data acquired in the proposed instrument are the outputs of the focal plane array. The illumination is assumed to be quasi-monochromatic with tunable central frequency, ω, so that the data are proportional to the spectral density (see [11], Section 2.4.1) on the focal plane array and are acquired serially for multiple values of ω.

The relationship between the spectral density measured on the focal plane of the proposed instrument and the susceptibility of the object is derived below. The measured optical intensity $I(\mathbf{r},\omega)$ is given by the spectral density—the ensemble average of the square magnitude of the incident field in the frequency domain at a single point, i.e.,

$$I(\mathbf{r},\omega) = \langle E^*(\mathbf{r},\omega)\, E(\mathbf{r},\omega)\rangle, \tag{1}$$

with the brackets, < >, denoting ensemble average.

From Fig. 1 it can be seen that the data are collected on a plane, with a two-dimensional position given by $\boldsymbol{\rho}$. The detected field is the superposition of a reference field E_r and a field E_s that is backscattered from the sample. As a result, the detected spectral density of Eq. (1) can be expressed as

$$\begin{aligned} I(\rho,k) &= \left\langle |E_r(\rho,k)+E_s(\rho,k)|^2 \right\rangle \\ &= \left\langle |E_r(\rho,k)|^2 + 2\ \mathrm{Re}\{E_r^*(\rho,k)\,E_s(\rho,k)\} + |E_s(\rho,k)|^2 \right\rangle, \end{aligned} \tag{2}$$

where $k=\omega/c$ in free space. More complicated dispersion relations for $k(\omega)$ may also be employed for propagation in dispersive media [37], but are not considered here.

The function $I(\boldsymbol{\rho}, k)$ may be seen to be the sum of three terms: a background term independent of the object; an autocorrelation term that is second-order in the scattered field; and the real part of the desired signal S, where

$$S(\rho,k)=\langle E_r^*(\rho,k)\,E_s(\rho,k)\rangle. \tag{3}$$

It is assumed that the background term, for the assumed form of the incident field, is independent of $\boldsymbol{\rho}$ and may be subtracted in a calibration stage. The autocorrelation term is neglected because the object is assumed to be weakly scattering (see [6] for a discussion of the performance of ISAM in relation to the autocorrelation artifact). The remaining term is proportional to the real part of the desired signal S.

From Eq. (3) it can be seen that the signal S is a cross correlation function. Taking the Fourier transform with respect to k allows this correlation to be expressed in the spatial domain as

$$\widehat{S}(\rho,\Delta z)=\left\langle \widehat{E}_r^*(\rho,z-\Delta z)\,\widehat{E}_s(\rho,z)\right\rangle. \tag{4}$$

The optical path in the reference arm of the instrument can be set so that

$$\widehat{S}(\rho,\Delta z)=0,\quad \forall\quad \Delta z<0. \tag{5}$$

This condition corresponds to an optical path in the reference arm that is shorter than the minimum optical path in the sample arm by at least the reciprocal of the source bandwidth (in wavenumbers). The condition on $\hat{S}$ given in Eq. (5) ensures that the real and imaginary parts of S are related by a Hilbert transform. As a result, the imaginary part of the data S can be calculated from the real part [6,38].

The observable quantity S must be related to the object, illumination source, and instrumentation to complete the forward model. To do this it is necessary to define the reference field E_r and the scattered field E_s seen in Eq. (3).

Let the field at the source field plane of Fig. 1 be given by $E_0\boldsymbol{\rho}, k)$. Note that the transverse position $\boldsymbol{\rho}$ is used to describe positions on the source plane and on the detector plane, as the former is imaged onto the latter. The field incident on the object is then given by

$$E_i(\mathbf{r},k)=\int \mathrm{d}^2\rho E_0(\rho,k)\,\mathcal{G}_{i0}(\mathbf{r}_\parallel,\rho;z,k), \tag{6}$$

where $\mathbf{r}$ is the position in the object, $\mathbf{r}_\parallel$ is the transverse component of $\mathbf{r}$, z is the component of $\mathbf{r}$ orthogonal to $\mathbf{r}_\parallel$, and $\mathcal{G}_{i0}$ is the Green's function describing propagation of light with wavenumber k from the source plane to the transverse plane at z.

Scattering from the object is governed by the susceptibility η, which is assumed to be independent of the wave-number k over the bandwidth of the system. Scattering is treated within the first Born approximation. As a result, a scattered field $k^2\eta(\mathbf{r})E_i(\mathbf{r},k)$ is produced within the object. This field propagates back through the instrument to give the field E_s at the detector. This field is therefore

$$\begin{aligned} E_s(\rho,k) &= \int \mathrm{d}^3 r \left[k^2 \eta(\mathbf{r}) E_i(\mathbf{r},k) \right] \mathcal{G}_{0i}(\rho, \mathbf{r}_\parallel; z, k) \\ &= k^2 \int \mathrm{d}^3 r \int \mathrm{d}^2 \rho' E_0\left(\rho', k\right) \times \mathcal{G}_{i0}\left(\mathbf{r}_\parallel, \rho'; z, k\right) \mathcal{G}_{0i}(\rho, \mathbf{r}_\parallel; z, k) \eta(\mathbf{r}), \end{aligned} \tag{7}$$

where $\mathcal{G}_{0i}$ describes propagation from the z plane in the object to the detector plane. This propagation operation to position $\boldsymbol{\rho}$ on the detector plane is equivalent to propagation to the position $\boldsymbol{\rho}$ on the source plane.

By reciprocity [39], $\mathcal{G}_{0i}$ and $\mathcal{G}_{i0}$ are related via

$$\mathcal{G}_{0i}(\rho, \mathbf{r}_\parallel; z, k) = \mathcal{G}_{i0}(\mathbf{r}_\parallel, \rho; z, k). \tag{8}$$

Furthermore, the mapping of the source into the sample will be assumed to be shift invariant across the relevant field of view, so that

$$\mathcal{G}_{i0}(\mathbf{r}_\parallel, \rho; z, k) = g\left(\mathbf{r}_\parallel - \frac{\rho}{M}; z, k\right), \tag{9}$$

where M is the magnification of the telescope and g is the normalized-unit point spread function (PSF) for illumination to plane z at wavenumber k. The telecentric optics in the sample arm ensure that the magnification M is not a function of z.

Substituting Eqs. (8) and (9) into Eq. (7) results in

$$E_s(\rho,k) = k^2 \int \mathrm{d}^3 r \int \mathrm{d}^2 \rho' E_0\left(\rho', k\right) g\left(\mathbf{r}_\parallel - \tfrac{\rho'}{M}; z, k\right) \times g\left(\mathbf{r}_\parallel - \tfrac{\rho}{M}; z, k\right) \eta(\mathbf{r}). \tag{10}$$

Returning to the definition of S [Eq. (3)], it can be seen that the data are the correlations between the backscattered and the reference fields. The reference field is an image of the source, as seen in Fig. 1. It will be assumed that the pupil used in the telecentric sample-arm telescope results in a significantly lower resolution than achieved in the reference arm. This leads to the approximation

$$S(\rho,k) = \left\langle E_r^*(\rho,k) E_s(\rho,k) \right\rangle \approx \left\langle E_0^*(\rho,k) E_s(\rho,k) \right\rangle. \tag{11}$$

Substituting into Eq. (10),

$$S(\rho,k) = \frac{k^2}{M^2} \int \mathrm{d}^3 r \int \mathrm{d}^2 \rho' W\left(\tfrac{\rho'}{M}, \tfrac{\rho}{M}; k\right) g\left(\mathbf{r}_\parallel - \tfrac{\rho'}{M}; z, k\right) \times g\left(\mathbf{r}_\parallel - \tfrac{\rho}{M}; z, k\right) \eta(\mathbf{r}), \tag{12}$$

where W is the demagnified cross-spectral density (see Ref. [11], Section 4.3.2)

$$W\left(\rho', \rho; k\right) = M^2 \left\langle E_0^*(M\rho, k), E_0\left(M\rho', k\right) \right\rangle. \tag{13}$$

It will be assumed that the coherence of the source field is spatially invariant and that the intensity of the illuminating field E_i is constant over the extent of the object. These assumptions allow the cross-spectral density to be expressed as a homogeneous Schell-model source (see Ref. [11], Section 5.3.2),

$$W\left(\rho',\rho;k\right)=A\left(k\right)b\left(\rho'-\rho;k\right). \tag{14}$$

Equation (14) can be used to simplify the expression for the data seen in Eq. (12). Denoting convolution over the transverse axes by *, and separating the three-dimensional position **r** into transverse and axial components $\mathbf{r}_\parallel$ and z,

$$S\left(\rho,k\right)=k^2A\left(k\right)\int\mathrm{d}z\int d^2r_\parallel\left[b*g\right]\left(\mathbf{r}_\parallel-\tfrac{\rho}{M};z,k\right)\times g\left(\mathbf{r}_\parallel-\tfrac{\rho}{M};z,k\right)\eta\left(\mathbf{r}_\parallel;z\right). \tag{15}$$

The second integral above can also be recognized as a two-dimensional convolution, giving

$$S\left(\rho,k\right)=\int\mathrm{d}z\left[h*\eta\right]\left(\tfrac{\rho}{M};z,k\right), \tag{16}$$

where

$$h\left(-\mathbf{r}_\parallel;z,k\right)=k^2A\left(k\right)\left[b*g\right]\left(\mathbf{r}_\parallel;z,k\right)g\left(\mathbf{r}_\parallel;z,k\right). \tag{17}$$

Equations (16) and (17) show that each transverse plane affects the data via a different PSF. The PSF for each plane is determined by the focusing optics (through g) and the source coherence properties (through b). In Eq. (17) the factor $b*g$ can be identified with the illuminating field and the factor g can be associated with detection of the scattered light.

The function g represents the field produced in the sample for a point source at the origin of the source plane. Thus the PSFs at different transverse planes are related by the laws of electromagnetic propagation. A field propagating in a homogenous medium can be expressed in an angular spectrum decomposition [40],

$$g\left(\mathbf{r}_\parallel;z,k\right)=-\frac{i}{2\pi}\int\mathrm{d}^2q\frac{G(\mathbf{q}/k)}{k_z(\mathbf{q})}e^{i\left[\mathbf{q}\cdot\mathbf{r}_\parallel+k_z(\mathbf{q})z\right]}, \tag{18}$$

where

$$k_z\left(\mathbf{q}\right)=\sqrt{k^2-q^2}, \tag{19}$$

and z=0 is the focal plane. That the angular spectrum G is a function only of $\mathbf{q}/k$ reflects an assumption of achromatic focusing. Note that the following analysis could easily be generalized to include chromatic optics.

Expressing the forward model in the Fourier domain is useful in the derivation of the ISAM data processing. From Eq. (18) it can be seen that the two-dimensional Fourier transform of g is

$$\tilde{g}(\mathbf{q};z,k) = -2\pi i \frac{G(\mathbf{q}/k)}{k_z(\mathbf{q})} e^{ik_z(\mathbf{q})z}. \tag{20}$$

The transfer function $\tilde{h}$ can then be found as the Fourier transform of Eq. (17),

$$\tilde{h}(-\mathbf{q};z,k) = -4\pi^2 k^2 A(k) \int \mathrm{d}^2 q' B\left(\mathbf{q}';k\right) \times \frac{G\left(\mathbf{q}'/k\right)}{k_z\left(\mathbf{q}'\right)} \frac{G\left[\left(\mathbf{q}-\mathbf{q}'\right)/k\right]}{k_z\left(\mathbf{q}-\mathbf{q}'\right)} e^{i\left[k_z\left(\mathbf{q}'\right)+k_z\left(\mathbf{q}-\mathbf{q}'\right)\right]z}, \tag{21}$$

where $B(\mathbf{q};k)$ is the Fourier transform of $b(\boldsymbol{\rho});k)$.

This transfer function $\tilde{h}$ can be used to take Eq. (16) into the Fourier domain:

$$\tilde{S}(-\mathbf{q};k) = -4\pi^2 k^2 M^2 A(k) \int \mathrm{d}z \int \mathrm{d}^2 q' B\left(\mathbf{q}';k\right) \times \frac{G\left(\mathbf{q}'/k\right) G\left[\left(M\mathbf{q}-\mathbf{q}'\right)/k\right]}{k_z\left(\mathbf{q}'\right) k_z\left(M\mathbf{q}-\mathbf{q}'\right)} \tilde{\eta}(-M\mathbf{q};z) \times e^{i\left[k_z\left(\mathbf{q}'\right)+k_z\left(M\mathbf{q}-\mathbf{q}'\right)\right]z}. \tag{22}$$

The exponential factor can be regarded as a Fourier kernel, giving

$$\tilde{S}(-\mathbf{q};k) = -4\pi^2 k^2 M^2 A(k) \int \mathrm{d}^2 q' B\left(\mathbf{q}';k\right) \times \frac{G\left(\mathbf{q}'/k\right) G\left[\left(M\mathbf{q}-\mathbf{q}'\right)/k\right]}{k_z\left(\mathbf{q}'\right) k_z\left(M\mathbf{q}-\mathbf{q}'\right)} \times \tilde{\tilde{\eta}}\left\{-M\mathbf{q}; -\left[k_z\left(\mathbf{q}'\right)+k_z\left(M\mathbf{q}-\mathbf{q}'\right)\right]\right\}, \tag{23}$$

where $\tilde{\tilde{\eta}}$ is the three-dimensional Fourier transform of the susceptibility. Equation (23) represents the most general Fourier-domain model for the partially coherent ISAM system.

B. Coherent Illumination

A limiting illumination case occurs when the source field is fully coherent. This can be achieved by reducing the iris in Fig. 1 to a pointlike aperture, giving a fully coherent plane wave at the source field plane. The case of full-field plane-wave illumination was considered in an earlier paper [8] and can be recovered here by setting $W(\boldsymbol{\rho},\boldsymbol{\rho}',k)=k^2A(k)$, i.e., full spatial coherence. This gives $B(\mathbf{q};k)=4\pi^2\delta(\mathbf{q}/k)$ and Eq. (21) reduces to

$$\tilde{h}(-\mathbf{q};z,k) = -16\pi^4 k^2 A(k) \frac{G(0)}{k} \frac{G[\mathbf{q}/k]}{k_z(\mathbf{q})} e^{i[k+k_z(\mathbf{q})]z}. \tag{24}$$

The Fourier-domain forward model is then [cf. Eq. (23)]

$$\tilde{S}(-\mathbf{q};k) = -16\pi^4 k M^2 A(k) G(0) \frac{G(M\mathbf{q}/k)}{k_z(M\mathbf{q})} \times \tilde{\tilde{\eta}}\{-M\mathbf{q}; -[k+k_z(M\mathbf{q})]\}. \tag{25}$$

This equation is the same as the result from [8] [Eq. (6) in that work] up to constant prefactors. The prefactors differ due to small differences in the definitions of the physical properties of the system.

C. Incoherent Illumination

The other limiting-case source statistics are achieved for an incoherent source. In this case no two points on the source plane are correlated, giving $W(\boldsymbol{\rho},\boldsymbol{\rho}',k)=k^2A(k)\delta[k(\boldsymbol{\rho}'-\boldsymbol{\rho})]$, and hence $B(\mathbf{q};k)=1$. An incoherent source can be realized by opening the iris seen in Fig. 1 very wide.

For an incoherent source, the transfer function of Eq. (21) becomes

$$\tilde{h}(-\mathbf{q};z,k)=-4\pi^2k^2A(k)\int \mathrm{d}^2q'\,\frac{G\left(\mathbf{q}'/k\right)}{k_z\left(\mathbf{q}'\right)}\frac{G\left[\left(\mathbf{q}-\mathbf{q}'\right)/k\right]}{k_z\left(\mathbf{q}-\mathbf{q}'\right)}\times e^{i\left[k_z\left(\mathbf{q}'\right)+k_z\left(\mathbf{q}-\mathbf{q}'\right)\right]z}. \tag{26}$$

The equation above is identical to the transfer function describing a single-objective confocal scanned-beam OCT system [see [4], Eq. (29)]. This equivalence can be physically justified. In the case of scanned-beam OCT, a focused beam is scanned transversely through the sample. Data measured at each transverse position of the beam are taken at different times, so that there is no interference between the fields produced for different scan positions. In the case of incoherent illumination, the illuminating field may be considered to consist of a superposition of mutually incoherent beams distributed in the transverse direction, each of which is analogous to a transverse position of the beam in the scanned-beam case. While the component beams all illuminate the object simultaneously, the light of one beam, scattered by the object, does not interfere with the light of other constituent beams. Therefore, while the scattered fields from many component beams overlap on the focal plane array, they do not interfere, and act as if each beam illuminated the object sequentially, rather than simultaneously. The same data may be recorded by replacing the incoherent source with a transversely scanned beam with the same spot size as that of the component beams of the incoherent illumination.

The results discussed above demonstrate that, by controlling source coherence, the full-field instrument may produce data similar to those that can be acquired with the scanned-beam implementations, but in a highly parallel fashion. It is important to note that even absent the solution of the inverse problem, the result is of considerable importance for full-field OCT because it provides a means to mitigate cross-talk artifacts that limit the utility of that modality. This point is expanded upon in Section 4.

3. APPROXIMATE MODELS AND INVERSE SCATTERING

The central enabling concept behind ISAM technology is the application of inverse scattering algorithms to the collected data. The benefit of applying inverse scattering algorithms is that regions that are regarded as out of focus in OCT are brought into diffraction-limited resolution. In both the full-field [8] and confocal cases [1,4], the inverse scattering algorithms reduce to linear filtering and Fourier resampling operations. The reduction to these simple procedures requires approximations to the forward model but allows real time implementation [9]. Experimental and computational studies have shown excellent imaging fidelity despite the use of approximations in the derivation of the ISAM inverse scattering algorithms [1,4].

As shown in Section 2, varying the source coherence in the partially coherent ISAM system allows a transition from full-field to confocal operation. In this section the inverse scattering algorithms for partially coherent ISAM will be derived. In one limit this inverse scattering is identical to the inverse scattering for the full-field system and in the other limit it reduces to the confocal ISAM inverse processing. The intermediate regime will also be examined, with the result that the ISAM Fourier-domain resampling varies as a function of the source coherence.

As shown in [4], the physical phenomena behind confocal ISAM are fundamentally different depending on whether the imaged region can be characterized as near the focal plane or far from the focal plane. Fortuitously, for a single-objective system the ISAM Fourier-domain re-sampling is the same in either case, meaning that the near-focus and far-from-focus inverse scattering algorithms are compatible. By contrast, full-field ISAM inverse scattering [8] has only a single region of operation but a Fourier resampling that is different from the confocal case. For partially coherent illumination in the system illustrated in Fig. 1, there are again two regions of operation (as in the confocal case) but in this case the Fourier resampling schemes are not commensurate across the regions.

Both the near-focus and far-from-focus cases for partially coherent ISAM are discussed below. However, this work will focus primarily on the near-focus regime for two reasons: first, the signal returned from the near-focus region is generally higher than from the out-of-focus region; and second, the source coherence can be adjusted so as to extend the near-focus region. The simulations shown in Section 5 provide further justification for the use of near-focus inverse scattering.

A. Near-Focus Operation

The near-focus ISAM scattering model is found by applying a simplifying assumption to the transfer function of Eq. (21) in the limit of a slowly varying exponential factor. This exponential will be slowly varying for regions near the focal plane [4].

To apply the approximation, it is necessary to assume forms for B and G. Here it will be assumed that the pupil has a Gaussian distribution so that

$$G(\mathbf{q}/k) = \exp\left(-\frac{\alpha^2 q^2}{2k^2}\right), \tag{27}$$

where the parameter $\alpha = \sqrt{2}/\mathrm{NA}$, and NA is the numerical aperture of the lens.

The coherence of the source is described by B which is of the form

$$B(\mathbf{q};k) = \frac{1}{\chi}\frac{\alpha^2}{2\pi}\exp\left(-\frac{1-\chi}{\chi}\frac{\alpha^2 q^2}{2k^2}\right). \tag{28}$$

As with the pupil, the source coherence function is defined to be Gaussian. Consequently, both the coherence profile in a plane and the angular distribution of light emerging from the source have a Gaussian distribution. The coherence profile is referenced to the objective aperture through the parameter α and the coherence length is controlled by the parameter χ. This form for B means that the coherence length on the source plane is $\sqrt{(1-\chi)/\chi}M\alpha/k$. For the case when $\chi=0$, $B(\mathbf{q};k)=\delta(\mathbf{q}/k)$ and coherent illumination is described. When $\chi=1$, $B(\mathbf{q};k)=\alpha^2/(2\pi)=1/(\pi NA^2)$, describing aperture-area-normalized incoherent illumination. All intermediate values of χ describe a partially coherent source. Physically, the parameter χ can be controlled with the iris illustrated in Fig. 1 or, for example, by the choice of diffuser used in conjunction with a spatially coherent source. It should be noted that the coherence length scales with the wavelength. This scaling property results in an angular divergence from the source that is independent of k, a fact evidenced by the dependence of B on q/k.

As described in [4], the factor $B(\mathbf{q}';k)G(\mathbf{q}'/k)G[(\mathbf{q}-\mathbf{q}')/k]$ appearing in the integrand of $\tilde{h}$ [Eq. (21)] will be peaked around some point $\mathbf{p}'$ in $\mathbf{q}'$ space. The remaining factors in Eq. (21) will be expanded in a Taylor series about $\mathbf{p}'$ and all but the leading term discarded. This results in

$$\tilde{h}(-\mathbf{q};z,k) \approx -4\pi^2 k^2 A(k) \frac{e^{i\left[k_z(\mathbf{p}')+k_z(\mathbf{q}-\mathbf{p}')\right]z}}{k_z(\mathbf{p}')k_z(\mathbf{q}-\mathbf{p}')} \int \mathrm{d}^2 q' B(\mathbf{q}';k) \times G\left(\frac{\mathbf{q}'}{k}\right) G\left(\frac{\mathbf{q}-\mathbf{q}'}{k}\right). \tag{29}$$

Given Eqs. (27) and (28) the integral above can be evaluated and the Taylor expansion point shown to be $\mathbf{p}'=\mathbf{q}\chi/(1+\alpha)$. The transfer function then becomes

$$\tilde{h}(-\mathbf{q};z,k) \approx -4\pi^2 k^2 A(k) \times \frac{\exp\left\{i\left[k_z\left(\frac{\mathbf{q}\chi}{1+\chi}\right)+k_z\left(\frac{\mathbf{q}}{1+\chi}\right)\right]z\right\}}{k_z\left(\frac{\mathbf{q}\chi}{1+\chi}\right)k_z\left(\frac{\mathbf{q}}{1+\chi}\right)} \times \frac{k^2}{1+\chi} \exp\left(-\frac{\alpha^2 q^2}{2k^2(1+\chi)}\right). \tag{30}$$

From this expression and the forward model relation of Eq. (16), it can be seen that the Fourier-domain forward model is

$$S(-\mathbf{q};k) = C(\mathbf{q};k)\tilde{\tilde{\eta}}(-M\mathbf{q};\beta(\mathbf{q};k)), \tag{31}$$

where

$$C(\mathbf{q};k) = \frac{-4\pi^2 k^4 M^2 A(k)}{(1+\chi)k_z\left(\frac{M\mathbf{q}\chi}{1+\chi}\right)k_z\left(\frac{M\mathbf{q}}{1+\chi}\right)} \exp\left(-\frac{\alpha^2 M q^2}{2k^2(1+\chi)}\right), \tag{32}$$

$$\beta(\mathbf{q};k) = -k_z\left(\frac{M\mathbf{q}\chi}{1+\chi}\right) - k_z\left(\frac{M\mathbf{q}}{1+\chi}\right). \tag{33}$$

The benefit of the approximation made in Eq. (29) is that the multiplex model of Eq. (23) is reduced to a one-to-one mapping between the object Fourier space and the data Fourier space, as seen in Eq. (31). That is, within the validity of the near-focus approximation, data collected at transverse Fourier component $\mathbf{q}$ and wavenumber k depend only on the three-dimensional Fourier transform of the object at $(M\mathbf{q},\beta)$. This relation is illustrated in Fig. 2, where the surfaces shown represent the locus of points in the Fourier-domain susceptibility that affect the data collected at wavenumber k.

B. Far-from-Focus Operation

The integral giving the transfer function $\tilde{h}$ in Eq. (21) contains an exponential factor that will be rapidly oscillating over $\mathbf{q}'$, for large values of $|kz|$. Large values of $|kz|$ describe regions away from the focus. For these far-from-focus regions the approximation of Eq. (29) is not appropriate, as the oscillatory exponential is not well-represented by only the first term of its Taylor series.

As described in [4], the stationary phase method (see [11], Section 3.C) can be used to approximate $\tilde{h}$. The stationary point is the value of $\mathbf{q}'$ at which the gradient of the exponential

argument is zero. Here the stationary point can be seen to be $\mathbf{q}'=\mathbf{q}/2$. This results in the far-from-focus approximation

$$\tilde{h}(-\mathbf{q};z,k) \approx -4\pi^2 k^2 A(k) \frac{\pi i}{kz} e^{i2k_z(\mathbf{q}/2)z} B\left(\frac{\mathbf{q}}{2};k\right) G\left(\frac{\mathbf{q}}{2k}\right) \times G\left(\frac{\mathbf{q}}{2k}\right). \tag{34}$$

Thus the far-from-focus model can also be written in the form

$$S(-\mathbf{q};k) = C'(\mathbf{q};k)\, \tilde{\tilde{\eta}}'\left(-M\mathbf{q};\beta'(\mathbf{q};k)\right), \tag{35}$$

where

$$\tilde{\tilde{\eta}}'(\mathbf{q},\beta) = \int \mathrm{d}z \frac{\tilde{\eta}(\mathbf{q},z)}{kz} e^{-i\beta z}, \tag{36}$$

is the Fourier transform of an axially attenuated object,

$$\beta'(\mathbf{q};k) = -2k_z\left(\frac{M\mathbf{q}}{2}\right), \tag{37}$$

and C' describes the system bandpass, which in this example is

$$C'(\mathbf{q};k) = \frac{-i2\pi^2 k^2 M^2 \alpha^2 A(k)}{\chi} \exp\left(-\frac{\alpha^2 M(1+\chi) q^2}{8k^2\chi}\right). \tag{38}$$

This far-from-focus model has several significant differences when compared to the near-focus model of Eqs. (31)–(33). Equation (36) includes a linear attenuation given by the distance from focus. This describes a decrease in signal power for scatterers away from the focus. The resampling described in Eq. (37) differs from the near-focus of Eq. (33) in that it is not a function of the coherence parameter χ. As described in [4], the near-focus and far-from-focus forms of β and α' are equal in the confocal–incoherent case, meaning that the same ISAM resampling can be applied in either region. For $\chi \neq 1$ the expression the expressions for β and β' are not equal, suggesting the use of different inverse scattering procedures depending on whether a scatterer is near focus or far from focus.

C. Near-Focus to Far-from-Focus Transition

For the full-field–coherent system, the near-focus approximation of Subsection 3.A is exact, meaning that there is no far-from-focus regime. In the confocal–incoherent system the near-focus to far-from-focus transition occurs at one Rayleigh range [4] but the Fourier domain resampling in each region is equal. As discussed above, the behavior is more complicated for a partially coherent source, i.e., $0<\chi<1$.

The transition between the near-focus and far-from-focus regimes can be found by considering a point scatterer at the plane z. The expected data may be evaluated for both regimes and the signal strength compared. Using the results from Subsections 3.A and 3.B it may be seen that the magnitudes of the signals are equal at the plane

$$|z_t| = \frac{1+\chi}{2\chi}\frac{\alpha^2}{k} = \frac{1+\chi}{2\chi}\frac{\lambda}{\pi NA^2}. \tag{39}$$

The factor $\lambda/(\pi NA^2)$ may be recognized as the Rayleigh range. Consistent with previous results, the transition plane z_t may be seen to be one Rayleigh range for the confocal/incoherent operation (χ=1) and at infinity for the full-field/coherent operation (χ=0).

The Fourier-domain resampling (β or β') varies between near-focus and far-from-focus regimes. Here it is suggested that the near-focus expression of Eq. (33) can be used in most instances–for high-coherence sources the near-focus region is large, and for low-coherence sources Eq. (37) approximates Eq. (33). This claim will be revisited in the numerical simulations of Section 5.

D. Inverse Scattering

Given the approximated model of Eq. (31), ISAM inverse scattering can be easily described and applied in real time [9]. The algorithm can be split into two distinct parts–filtering and resampling.

The filtering operation ameliorates the effects of noise and, as far as possible, undoes the effects of C in Eq. (31). The linear filtering operation can be realized by a Fourier-domain multiplication with some function C^+, i.e., the processed data are

$$S^+(-\mathbf{q}, k) = C^+(\mathbf{q};k)\, S(-\mathbf{q}, k). \tag{40}$$

This inversion filter is designed to undo the effects of C without introducing instabilities in the presence of noise. There are a variety of standard methods to define C^+, with perhaps the most famous being the Wiener filter [41]. A simple version of the Wiener filter is

$$C^+(\mathbf{q};k) = \frac{C^*(\mathbf{q};k)}{|C(\mathbf{q};k)|^2 + \gamma^2}, \tag{41}$$

where γ is a regularization parameter used to limit the value of C^+ and thus provide stability in the presence of noise.

The resampling operation involves warping the processed data S^+ in Fourier space so as to undo the effects of the imaging system. In Eq. (31) it can be seen that the Fourier-domain data is proportional to the three-dimensional Fourier transform of the object defined on a distorted coordinate system. The distortion is given by Eq. (33) and is illustrated in Fig. 2. By applying a one-dimensional interpolation at each $\mathbf{q}$ point, the mapping given by β can be undone. As seen in earlier work, this processing removes out-of-focus blurring.

In standard OCT the full β–k relation is not used to reconstruct the data. Rather, a scaled axial Fourier transform is used to take spectral-domain OCT data into the spatial domain. This operation is equivalent to $\beta(\mathbf{q};k) = -2k$; a poor approximation to Eq. (33).

4. MULTIPLE SCATTERING

In both OCT and ISAM data are processed under the assumption that only singly scattered light is present in the interferometric signal. As a result, any multiply scattered light appearing in the interferogram is a source of error. In confocal systems, much of the multiply scattered

light is rejected at the confocal pinhole. In general, multiple scattering is more problematic in full-field systems, where more multiply scattered light reaches a detector element. Multiple scattering in a full-field system is illustrated in Fig. 3. This section describes how multiple scattering can be modeled and how partial coherence of the source can be used to mitigate multiple-scattering artifacts. It should be noted that previous studies of confocal and full-field ISAM (e.g. [4,8]) did not explicitly consider multiple scattering effects.

As illustrated in Fig. 3, second-order scattering occurs when light from source position $\boldsymbol{\rho}'$ scatters from a position $\mathbf{r}'$ in the sample. This scattered light is scattered for a second time at $\mathbf{r}$ and subsequently propagates to the detector position $\boldsymbol{\rho}$. This process can be described mathematically in the same way that first-order scattering was described in Subsection 2.A. The source field E_0 is propagated into the sample by $\mathcal{G}_{i0}$, it scatterers in the object, and is propagated using the free-space Green's function $\mathcal{G}_f$. A second scattering event occurs in the object and propagation to the detector is given by $\mathcal{G}_{0i}$. The scattered field E_s at the detector is found by integrating over all source positions, and pairs of scattering locations, so that

$$E_s(\rho,k)=k^4\int \mathrm{d}^3r\int \mathrm{d}^3r'\int \mathrm{d}^2\rho' E_0\left(\rho',k\right)\mathcal{G}_{i0}\left(\mathbf{r}_{\|}',\rho';z',k\right)\times\eta\left(\mathbf{r}'\right)\mathcal{G}_f\left(\mathbf{r},\mathbf{r}';k\right)\eta(\mathbf{r})\,\mathcal{G}_{0i}(\rho,\mathbf{r}_{\|};z,k)\,. \tag{42}$$

This expression can be compared to the field due to single scattering seen in Eq. (7).

The free-space Green's function (see Ref. [11], Section 3.2.4) is

$$\mathcal{G}_f\left(\mathbf{r},\mathbf{r}';k\right)=\frac{\exp\left(ik|\mathbf{r}-\mathbf{r}'|\right)}{|\mathbf{r}-\mathbf{r}'|}. \tag{43}$$

Using this expression and Eqs. (8), (9), (11), and (13), Eq. (42) becomes

$$S(\rho,k)=\frac{k^4}{M^2}\int \mathrm{d}^3r\int \mathrm{d}^3r'\int \mathrm{d}^2\rho' W\left(\tfrac{\rho'}{M},\tfrac{\rho}{M};k\right)\times g\left(\mathbf{r}_{\|}'-\tfrac{\rho'}{M};z',k\right)\frac{\exp\left(ik|\mathbf{r}-\mathbf{r}'|\right)}{|\mathbf{r}-\mathbf{r}'|}\times g\left(\mathbf{r}_{\|}-\tfrac{\rho}{M};z,k\right)\eta(\mathbf{r})\,\eta\left(\mathbf{r}'\right). \tag{44}$$

This expression represents the second-order scattering contribution to the collected data [cf. the first-order contribution given by Eq. (12)].

To see how the partial coherence of the source field can be used to mitigate multiple-scattering effects, consider an object with strong scattering centers around $\mathbf{r}^{(1)}=\left(\mathbf{R}_{\|}^{(1)},0\right)$ and $\mathbf{r}^{(2)}=\left(\mathbf{R}_{\|}^{(2)},0\right)$. Since the focused field $g(\mathbf{r}_{\|};0,k)$ is significant only in a small region around $\mathbf{r}_{\|}=0$, multiple scattering from $\mathbf{r}^{(1)}$ to $\mathbf{r}^{(2)}$ will produce significant effects in the data only when $\rho'\approx M\mathbf{R}_{\|}^{(1)}$ and $\rho\approx M\mathbf{R}_{\|}^{(2)}$. This condition is illustrated in Fig. 3, where the scatterers lie in the focal regions corresponding to the points $\boldsymbol{\rho}$ and ρ on the source–detector plane. When this condition is satisfied the $\eta(\mathbf{r})$, $\eta(\mathbf{r}')$, $g\left(\mathbf{r}_{\|}'-\rho'/M;z',k\right)$ and $g(\mathbf{r}_{\|}-\rho/M;z,k)$ factors in Eq. (44) are simultaneously large around the volume of integration centered at $\mathbf{r}_{\|}'=\mathbf{R}_{\|}^{(1)}$ and $\mathbf{r}_{\|}=\mathbf{R}_{\|}^{(2)}$. The remaining factors in the integrand are the free-space Green's function and the cross-spectral density, which in the relevant region of the integration volume is approximately $W\left(\mathbf{R}_{\|}^{(1)},\mathbf{R}_{\|}^{(2)};k\right)$. For a fully coherent source this cross-spectral density is constant and does not

have an effect. As the source coherence is reduced, $W\left(\mathbf{R}_{\parallel}^{(1)}, \mathbf{R}_{\parallel}^{(2)}; k\right)$ introduces attenuation to the multiple-scattering contribution. As illustrated in Fig. 3, light from the source position $\boldsymbol{\rho}'$ can be doubly scattered primarily to the detector position ρ. If the source coherence length is less than $|\boldsymbol{\rho}' - \boldsymbol{\rho}|$, the interferometric visibility of the multiply scattered light is low and hence gives minimal contribution to the data. This process is in contrast to single scattering, where the light originating from $\boldsymbol{\rho}$ is primarily scattered to the vicinity of the same point $\boldsymbol{\rho}$ on the detector.

5. SIMULATIONS

The performance of partially coherent ISAM with regard to image reconstruction and rejection of multiple scattering can be investigated using numerical simulations. Synthetic single-scattering data are calculated by defining an object susceptibility η and evaluating Eq. (12). In this case the object is defined to be three identical point scatterers. Second-order-scattering data from each pair of points is generated using Eq. (44). Higher-order scattering is assumed to produce negligible signal in the simulations presented here.

Data are collected at 50 values of k, evenly spaced around $k=2\pi/\lambda$ (where λ is a fixed central wavelength) with a 25% bandwidth. The point scatterers in the object are located at (20,0,0)λ, (0,0,15)λ, and (–20,0,30)λ in Cartesian coordinates, where $z=0$ is the focal plane. A numerical aperture of 0.2 is assumed and the detector is modeled as having x–y extent of 70λ×30λ. Various values of the coherence parameter χ are simulated in order to demonstrate the effects of the partial coherence of the source.

As described in Subsection 3.D, an OCT image can be recovered by taking a scaled axial Fourier transform of the data. ISAM reconstructions are found using the near-focus model described in Subsection 3.A and the resampling approach described in Subsection 3.D. A linear filter [Eq. (40)] is not applied in these examples, so as to allow a clear comparison between OCT images and the results of the novel ISAM resampling scheme. ISAM and OCT images can be seen in Fig. 4—OCT images are seen in the left column and ISAM reconstructions in the right column. The data and images are complex functions on $\mathbb{R}^3$, so, to facilitate visualization, projections of the function magnitude over the y axis are shown.

The ideal reconstructed image would consist of three diffraction-limited spots at the locations of the point scatterers. The images of Fig. 4 contain structure, not diffraction-limited in all cases, at these locations, in addition to artifacts caused by multiple scattering. As the source coherence is decreased (i.e., as χ is increased) the effects of multiple scattering lessen, as expected. ISAM image reconstruction can be seen to result in sharp images of the point scatterers, at the correct locations. The ISAM processing does not necessarily produce diffraction-limited spots from the multiple-scattering artifacts, as the phase structure on these artifacts does not match the single-scattering patterns that ISAM is predicated on. A similar effect has been observed in the autocorrelation artifact [6], which ISAM is seen to blur.

As discussed in Section 3, the characteristics of the system differ depending on whether an imaged scatterer can be characterized as near-focus or far-from-focus. The transition point between these two regimes is described in Eq. (39) and depends on the coherence properties of the source and the focusing characteristics of the objective lens. For the examples shown in Fig. 4 the transition planes are $z_t=\infty$ (no far-from-focus region) for $\chi=0$, $z_t=2000\lambda$ for $\chi=0.002$, $z_t=400\lambda$ for $\chi=0.01$, and $z_t=12\lambda$ for $\chi=0.5$. The scatterer at (–20,0,30)λ is therefore in the far-from-focus region for the $\chi=0.5$ images of Figs. 4(g) and 4(h). This claim is supported by the lower reconstruction amplitude observed for this scatterer and predicted in the far-from-focus regime by Eq. (36). The ISAM Fourier-domain mapping also changes from near-focus to far-from focus, meaning that the use of the near-focus re-sampling to generate Fig. 4(h) introduces

an error. However, the far-from-focus scatterer is still reconstructed as pointlike, meaning that the error has minimal effect in this example.

In most scenarios the focal plane of the system is set to lie within the area of interest. This would suggest the use of the near-focus ISAM model of Subsection 3.A. The source coherence can then be set to minimize multiple-scatter artifacts while also giving a sufficiently large transition plane z_t so as to capture the region of interest. Ensuring the near-focus region encompasses the area of interest means that the near-focus model can be used with confidence and that the $1/(kz)$ loss in signal associated with far-from-focus operation does not adversely affect the signal-to-noise ratio. However there may be cases where it is desirable to have some, or all, of the object in the out-of-focus region. In this case the change in resampling schemes between near-focus and far-from-focus operation [see Eqs. (33) and (37)] can be minimized by selecting a large value of χ and/or using a low numerical aperture.

In summary, the simulations shown in Fig. 4 illustrate the main points of full-field ISAM: multiple scattering can produce artifacts corrupting the desired single-scatter signal; for the single-scatter signal, ISAM processing corrects the blurring observed in OCT outside the depth of focus; in general ISAM does not remove defocus in the multiple-scatter artifact; decreased spatial coherence of the source can be used to reduce the multiple-scatter artifact; and the near-focus model of Subsection 3.A, which is used to define the ISAM resampling here, is valid for multiple Rayleigh ranges, where the number of Rayleigh ranges decreases with decreasing source spatial coherence.

6. CONCLUSION

The coherence properties of the source of illumination in ISAM can play an important and useful role in image reconstruction. In both ISAM and OCT, decreasing the spatial coherence of the source helps reject multiple-scattering artifacts and can improve image quality. By varying the source coherence, the proposed ISAM instrument can behave as a full-field imaging system (full source coherence), as a parallelized confocal system (source incoherence), or in some intermediate regime (partial source coherence). The source coherence can be chosen by striking a balance between the competing goals of multiple-scatter rejection (improves with decreasing coherence) and a large axial imaging range over which the signal strength does not decrease (improves with increasing coherence). This depth over which the signal strength is constant [given by Eq. (39)] can be made many times larger than the Rayleigh range given a prudent choice of coherence properties. Unlike traditional OCT systems, which give diffraction-limited resolution over the Rayleigh range only, ISAM processing enables a diffraction-limited image to be achieved over this whole constant-signal volume. Furthermore, the use of physics-based image reconstruction algorithms means that a quantitative estimate of the susceptibility is obtained.

Acknowledgments

This work was supported in part by the National Institutes of Health (NIH) (Roadmap Initiative, NIBIB, 1 R21 EB005321, and NIBIB, 1 R01 EB005221 to S. A. Bop-part), the National Science Foundation (NSF) (CAREER Award BES 03-47747 and BES 05-19920, and BES 06-19257 to S. A. Boppart, and CAREER Award 0239265 to P. S. Carney), and the Grainger Foundation.

REFERENCES

1. Ralston TS, Marks DL, Carney PS, Boppart SA. Interferometric synthetic aperture microscopy. Nat. Phys 2007;5:129–134.
2. Davis BJ, Marks DL, Ralston TS, Carney PS, Boppart SA. Interferometric synthetic aperture microscopy: computed imaging for scanned coherent microscopy. Sensors 2008;8:3903–3931.

3. Ralston TS, Marks DL, Carney PS, Boppart SA. Inverse scattering for optical coherence tomography. J. Opt. Soc. Am. A 2006;23:1027–1037.
4. Davis BJ, Schlachter SC, Marks DL, Ralston TS, Boppart SA, Carney PS. Nonparaxial vector-field modeling of optical coherence tomography and interferometric synthetic aperture microscopy. J. Opt. Soc. Am. A 2007;24:2527–2542.
5. Ralston TS, Marks DL, Boppart SA, Carney PS. Inverse scattering for high-resolution interferometric microscopy. Opt. Lett 2006;31:3585–3587. [PubMed: 17130911]
6. Davis BJ, Ralston TS, Marks DL, Boppart SA, Carney PS. Autocorrelation artifacts in optical coherence tomography and interferometric synthetic aperture microscopy. Opt. Lett 2007;32:1441–1443. [PubMed: 17546148]
7. Marks DL, Ralston TS, Carney PS, Boppart SA. Inverse scattering for rotationally scanned optical coherence tomography. J. Opt. Soc. Am. A 2006;23:2433–2439.
8. Marks DL, Ralston TS, Boppart SA, Carney PS. Inverse scattering for frequency-scanned full-field optical coherence tomography. J. Opt. Soc. Am. A 2007;24:1034–1041.
9. Ralston TS, Marks DL, Carney PS, Boppart SA. Real-time interferometric synthetic aperture microscopy. Opt. Express 2008;16:2555–2569. [PubMed: 18542337]
10. Goodman, J. Statistical Optics. Wiley; 1985. p. 193-195.Chap. 5.3.3
11. Mandel, L.; Wolf, E. Optical Coherence and Quantum Optics. Cambridge U. Press; 1995.
12. Leitgeb R, Hitzenberger CK, Fercher AF. Performance of Fourier domain vs. time domain optical coherence tomography. Opt. Express 2003;11:889–894. [PubMed: 19461802]
13. Choma MA, Sarunic MV, Yang C, Izatt JA. Sensitivity advantage of swept source and Fourier domain optical coherence tomography. Opt. Express 2003;11:2183–2189. [PubMed: 19466106]
14. Akiba M, Chan KP, Tanno N. Full-field optical coherence tomography by two-dimensional heterodyne detection with a pair of CCD cameras. Opt. Lett 2003;28:816–818. [PubMed: 12779156]
15. Beaurepaire E, Boccara A-C. Full-field optical coherence microscopy. Opt. Lett 1998;23:244–246. [PubMed: 18084473]
16. Blazkiewicz P, Gourlay M, Tucker JR, Rakic AD, Zvyagin AV. Signal-to-noise ratio study of full-field Fourier-domain optical coherence tomography. Appl. Opt 2005;34:7722–7729. [PubMed: 16381518]
17. Dubois A, Vabre L, Boccara A-C, Beaurepaire E. High-resolution full-field optical coherence tomography with a Linnik microscope. Appl. Opt 2002;41:805–812. [PubMed: 11993929]
18. Dubois A, Moneron G, Grieve K, Boccara A-C. Three-dimensional cellular-level imaging using full-field optical coherence tomography. Phys. Med. Biol 2004;49:1227–1234. [PubMed: 15128200]
19. Grieve AK, Moneron G, Lecaque R, Vabre L, Boccara C. Ultrahigh-resolution full-field optical coherence tomography. Appl. Opt 2004;43:2874–2883. [PubMed: 15143811]
20. Grieve K, Dubois A, Simonutti M, Paques M, Sahel J, Le Gargasson J-F, Bocarra C. *In vivo* anterior segment imaging in the rat eye with high speed white light full-field optical coherence tomography. Opt. Express 2005;13:6286–6295. [PubMed: 19498641]
21. Grieve K, Moneron G, Dubois A, Le Gargasson J-F, Boccara C. Ultrahigh resolution *ex vivo* ocular imaging using ultrashort acquisition time *en face* optical coherence tomography. J. Opt. A, Pure Appl. Opt 2005;7:368–373.
22. Laude B, De Martino A, Drevillon B, Benattar L, Schwartz L. Full-field optical coherence tomography with thermal light. Appl. Opt 2002;41:6637–6645. [PubMed: 12412654]
23. Moneron G, Bocarra A-C, Dubois A. Stroboscopic ultrahigh-resolution full-field optical coherence tomography. Opt. Lett 2005;30:1351–1353. [PubMed: 15981530]
24. Moreau J, Lorlette V, Bocarra A-C. Full-field birefringence imaging by thermal-light polarization-sensitive optical coherence tomography. II. Instrument and results. Appl. Opt 2003;42:3811–3818. [PubMed: 12868819]
25. Watanabe Y, Hayasaka Y, Sato M, Tanno N. Full-field optical coherence tomography by achromatic phase shifting with a rotating polarizer. Appl. Opt 2005;44:1387–1392. [PubMed: 15796236]
26. Zvyagin AV. Fourier-domain optical coherence tomography: optimization of signal-to-noise ratio in full space. Opt. Commun 2004;242:97–108.

27. Zvyagin AV, Blazkiewicz P, Vintrou J. Image reconstruction in full-field Fourier-domain optical coherence tomography. J. Opt. A, Pure Appl. Opt 2005;7:350–356.
28. Povazay B, Unterhuber A, Hermann B, Sattmann H, Arthaber H, Drexler W. Full-field time-encoded frequency-domain optical coherence tomography. Opt. Express 2006;14:7661–7669. [PubMed: 19529134]
29. Dubois F, Joannes L, Legros J-C. Improved three-dimensional imaging with a digital holography microscope with a source of partial spatial coherence. Appl. Opt 1999;38:7085–7094. [PubMed: 18324255]
30. Dubois F, Requena M-LN, Minetti C, Monnom O, Istasse E. Partial spatial coherence effects in digital holographic microscopy with a laser source. Appl. Opt 2004;43:1131–1139. [PubMed: 15008493]
31. Yadlowsky MJ, Schmitt JM, Bonner RF. Multiple scattering in optical coherence tomography. Appl. Opt 1995;34:5699–5707.
32. Karamata B, Lambelet P, Laubscher M, Salathe RP, Lasser T. Spatially incoherent illumination as a mechanism for cross-talk suppression in wide-field coherence tomography. Opt. Lett 2004;29:736–738. [PubMed: 15072375]
33. Karamata B, Laubscher M, Leutenegger M, Bourquin S, Lasser T. Multiple scattering in optical coherence tomography. I. Investigation and modeling. J. Opt. Soc. Am. A 2005;22:1369–1379.
34. Karamata B, Leutenegger M, Laubscher M, Bourquin S, Lasser T. Multiple scattering in optical coherence tomography. II. Experimental and theoretical investigation of cross talk in wide-field optical coherence tomography. J. Opt. Soc. Am. A 2005;22:1380–1388.
35. Born, M.; Wolf, E. Principles of Optics. Cambridge U. Press; 1980. p. 524-526.Chap. 10.5.2
36. Chinn SR, Swanson EA, Fujimoto JG. Optical coherence tomography using a frequency-tunable optical source. Opt. Lett 1997;22:340–342. [PubMed: 18183195]
37. Marks DL, Oldenburg AL, Reynolds JJ, Boppart SA. A digital algorithm for dispersion correction in optical coherence tomography for homogeneous and stratified media. Appl. Opt 2003;42:204–217. [PubMed: 12546500]
38. Zhao Y, Chen Z, Saxer C, Xiang S, de Boer JF, Nelson JS. Phase-resolved optical coherence tomography and optical Doppler tomography for imaging blood flow in human skin with fast scanning speed and high velocity sensitivity. Opt. Lett 2000;25:114–116. [PubMed: 18059800]
39. Potton RJ. Reciprocity in optics. Rep. Prog. Phys 2004;67:717–754.
40. Wolf E. Electromagnetic diffraction in optical systems. I. An integral representation of the image field. Proc. R. Soc. London, Ser. A 1959;253:349–357.
41. Wiener, N. Extrapolation, Interpolation, and Smoothing of Stationary Time Series. MIT; 1964.

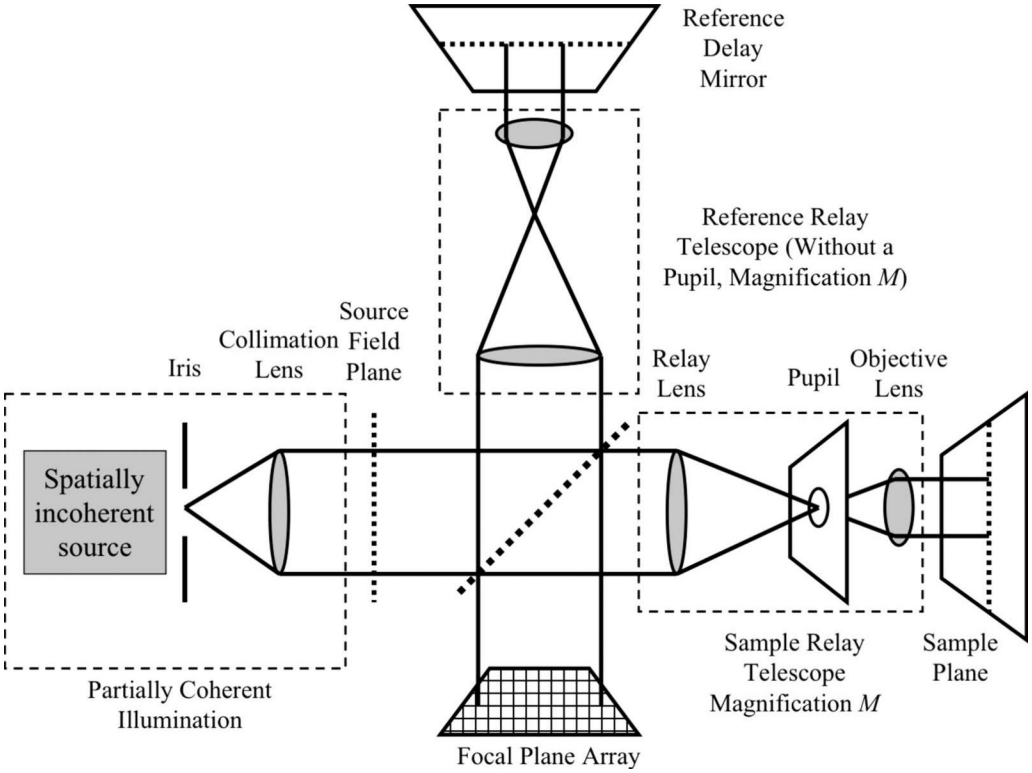

Fig. 1.
Diagram of full-field OCT instrument with a source of adjustable partial coherence.

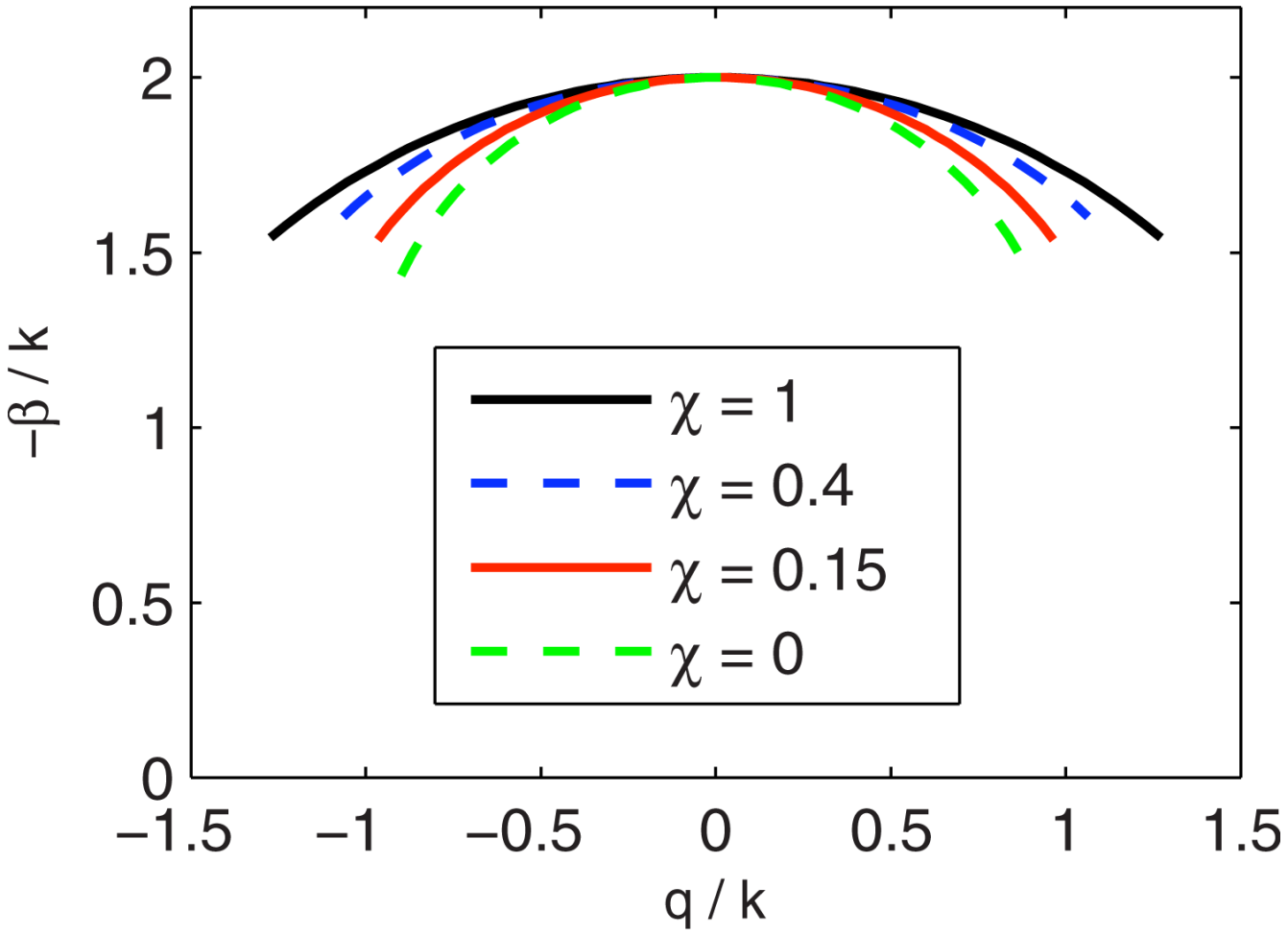

Fig. 2.

(Color online) Contours of the mapping ($\beta(\mathbf{q};k)$ for various coherence parameters χ. The transverse widths of the contours are representative of the bandwidth for a system with α=1.57 (NA=0.9). This bandwidth is determined by $C(\mathbf{q};k)$ [Eq. (32)]. Note that $\beta(\mathbf{q};k)$ is a function on the two-dimensional **q** plane, but varies only with the magnitude q, as plotted here.

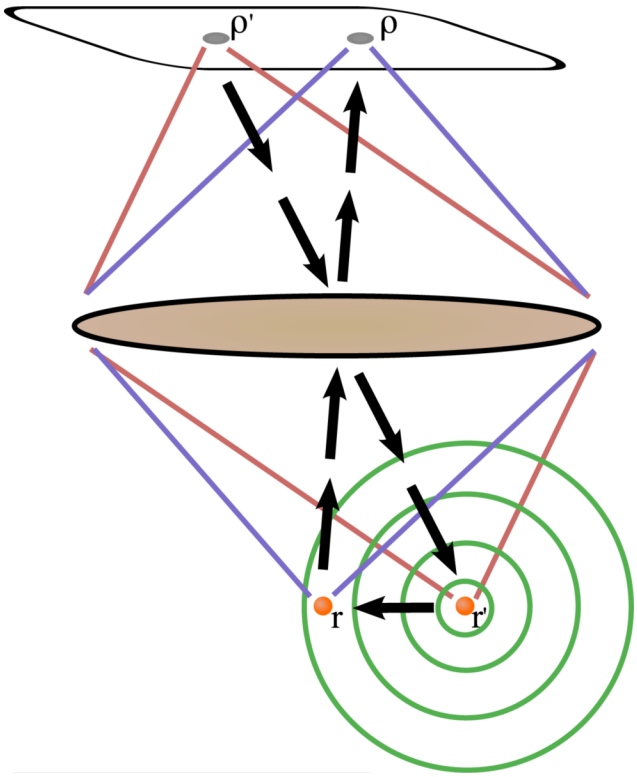

Fig. 3.
(Color online) An illustration of multiple scattering—in this case second-order scattering. Light from the source plane is focused into the sample, scatters twice, and is focused onto the detector. The reference-arm optics image the source plane onto the detector, so in this simplified diagram the source and detector planes are colocated.

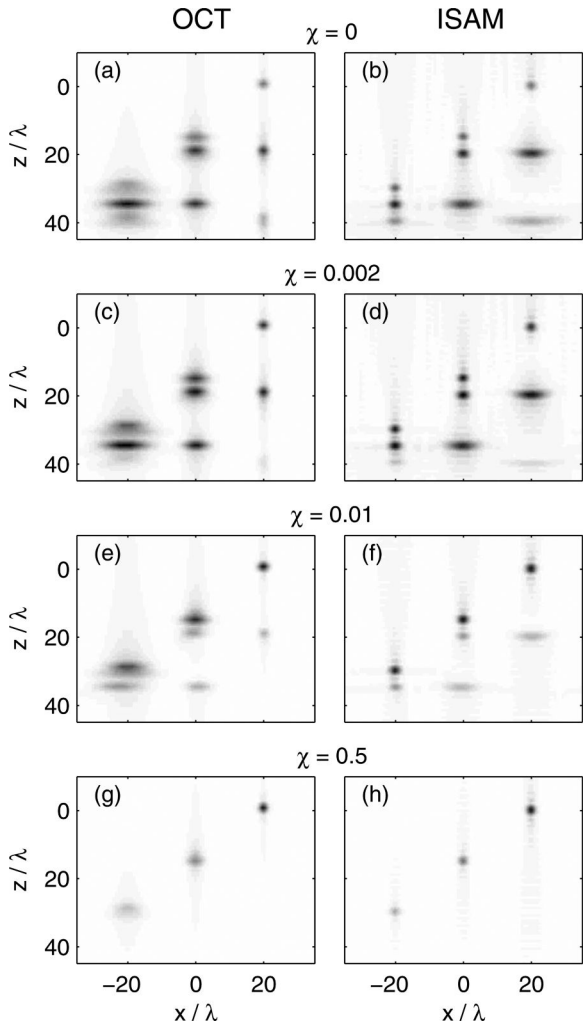

Fig. 4.

(a), (c), (e), (g) OCT and (b), (d), (f), (h) ISAM images of an object consisting of three point scatterers at (20,0,0)λ, (0,0,15)λ, and (–20,0,30)λ. The source spatial coherence is varied as described by the parameter χ, the numerical aperture of the objective is 0.2 and the focal plane is at z=0. The coherence lengths are (a), (b) ∞ (χ=0), (c), (d) 25λ (χ=0.002), (e), (f) 11λ (χ=0.01), and (g), (h) 1.1λ (χ=0.5). The images are formed from data consisting of first- and second-order scattering effects. A projection over the y axis of the three-dimensional image magnitudes is taken to produce the two-dimensional images displayed.